

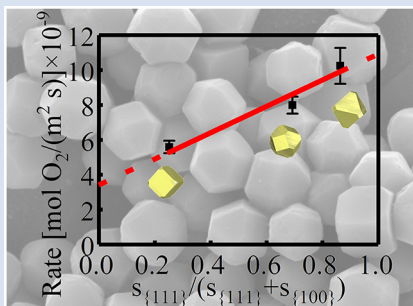
Morphology dominated rapid oxidation of framboidal pyrite

R. Du^{1,2,3}, H. Xian^{1,2*}, X. Wu^{1,2,3}, J. Zhu^{1,2}, J. Wei^{1,2,3},
J. Xing^{1,2,3}, W. Tan^{1,2}, H. He^{1,2,3}



doi: 10.7185/geochemlet.2104

Abstract



The rapid oxidation of framboidal pyrite is conventionally attributed to its fine grain size. However, the effect of the crystal facets of the microcrystals in the framboids on the oxidation process has been overlooked. We synthesised pyrite microcrystals of microscopic size with both {100} and {111} facets, which are two major forms of framboidal pyrite crystals, in order to examine the oxidation behaviour of pyrite framboids. The results showed that the oxidation rate of microcrystals with a greater proportion of {111} facets was approximately 2 times higher than that of those with a greater proportion of {100} facets although the latter's size was smaller. Such a difference makes framboidal pyrite with {111} facets more sensitive to oxidative weathering in geochemical cycles than other forms of pyrite. These findings emphasise the role of crystal anisotropy in controlling the oxidation of framboidal pyrite, thereby suggesting that the shape controlled oxidation of pyrite is a potential indicator of the local redox conditions of the palaeoenvironment where it occurred.

Received 10 June 2020 | Accepted 2 January 2021 | Published 9 February 2021

Introduction

Sedimentary sulfides account for more than 95 % of the sulfides on the surface of the Earth and mainly occur as pyrite in sediments (Rickard *et al.*, 2017). The formation and oxidative weathering of sedimentary pyrite are core processes in the sulfur cycle and are simultaneously involved in other major element cycles (such as carbon, nitrogen, and oxygen) (Hayakawa *et al.*, 2013; Fike *et al.*, 2015; Fakhraee *et al.*, 2019). Thus, these processes have regulated the redox conditions of the Earth's surface through geological history, especially oceanic redox conditions (Wang *et al.*, 2018). Changes in redox conditions also affect the distribution of elements (Anbar, 2008).

Framboidal pyrite, which is the main component and dominant pyrite texture of sedimentary pyrite (Wilkin *et al.*, 1996; Sawlowicz, 2000; Rickard, 2012), plays a major role in the oxidation of sedimentary pyrite. Billions of pyrite grains are forming in sediments and waterways worldwide every second (Ohfuji and Rickard, 2005; Rickard, 2015, 2019a,b). The oldest framboidal pyrite may be found in the late Archean (≤ 2.9 Ga) sediments. (Hallbauer, 1986; Guy *et al.*, 2010).

Pyrite is easily oxidised when exposed to the Earth's oxygenic atmosphere and oceans. The pyrite oxidation process has been investigated extensively for decades, particularly the reaction kinetics and oxidation mechanism. Most previous studies mainly focused on powder samples, *i.e.* fracture surfaces, and ignored crystal facet effects (Zhu *et al.*, 2018), which may have

hindered the accurate determination of the pyrite oxidation mechanism. Moreover, little attention has been paid to the oxidative behaviour of framboidal pyrite, despite its importance in sediments. The oxidation of framboidal pyrite is considered to be fast due to its high specific surface area (SSA) (Pugh *et al.*, 1984; Weber *et al.*, 2004), and the influence of the crystal shape is often neglected. Several studies have shown that framboidal pyrite grains are mostly euhedral microcrystals with specific shapes (mainly with {100} and {111} facets) (Ohfuji and Rickard, 2005; Rigby *et al.*, 2006; Kozina *et al.*, 2018). Poorly understood issues regarding the rapid oxidation of framboidal pyrite are what controls the oxidation processes; the unique crystal shape or the extremely fine crystal size?

Here, we investigated the surface oxidation behaviour of synthesised sub-micron pyrite with predominantly {100} or {111} facets. Our results showed that the specific crystal facet of the microscopic pyrite microcrystals, rather than the grain size, dominated its oxidation. Also, the shape controlled oxidation processes of pyrite as indicators of the local redox conditions of the palaeoenvironment are discussed.

Materials and Methods

Highly pure, specifically shaped microscopic pyrite samples were synthesised using a polymer assisted hydrothermal method, see [Supplementary Information \(SI\)](#). To induce oxidation reactions, the prepared pyrite films were exposed to humidity controlled air

1. CAS Key Laboratory of Mineralogy and Metallogeny/Guangdong Provincial Key Laboratory of Mineral Physics and Materials, Guangzhou Institute of Geochemistry, Chinese Academy of Sciences (CAS), Guangzhou 510640, China
2. CAS Center for Excellence in Deep Earth Science, Guangzhou 510640, China
3. University of Chinese Academy of Sciences, Beijing 100049, China
* Corresponding author (email: xianhaiyang@gig.ac.cn)



in airtight cells for 84 hr in total. During the oxidation process, the samples were removed for X-ray photoelectron spectroscopy (XPS) analysis at reaction intervals of 0, 6, 12, 24, 36, 60, and 84 hr. Details of the experimental procedures and characterisation methods are presented in the SI.

Results and Discussion

Structural, chemical and morphological analyses. No impurity reflections in the X-ray diffraction (XRD) patterns were identified, thereby confirming the high purity of the pyrite samples (Fig. 1a–c). In sample Py-tc (truncated cubic pyrite), the

(111) reflection was relatively weak while the (200) reflection was relatively strong. Compared with those of sample Py-co, the (111) reflections of samples Py-co (cubo-octahedral pyrite) and Py-to (truncated octahedral pyrite) were stronger, whereas the reflection of (200) was weaker.

Figure 1d–f presents the morphology of the three samples. The change in their morphology indicated that they possessed different proportions of cubic {100} and octahedral {111} facets, which was identical to the aforementioned XRD results. The energy dispersive spectrometry (EDS) results for all three samples, shown in Figure 1g–i, confirmed the chemical purity of the pyrite phases. It should be noted that there are weak

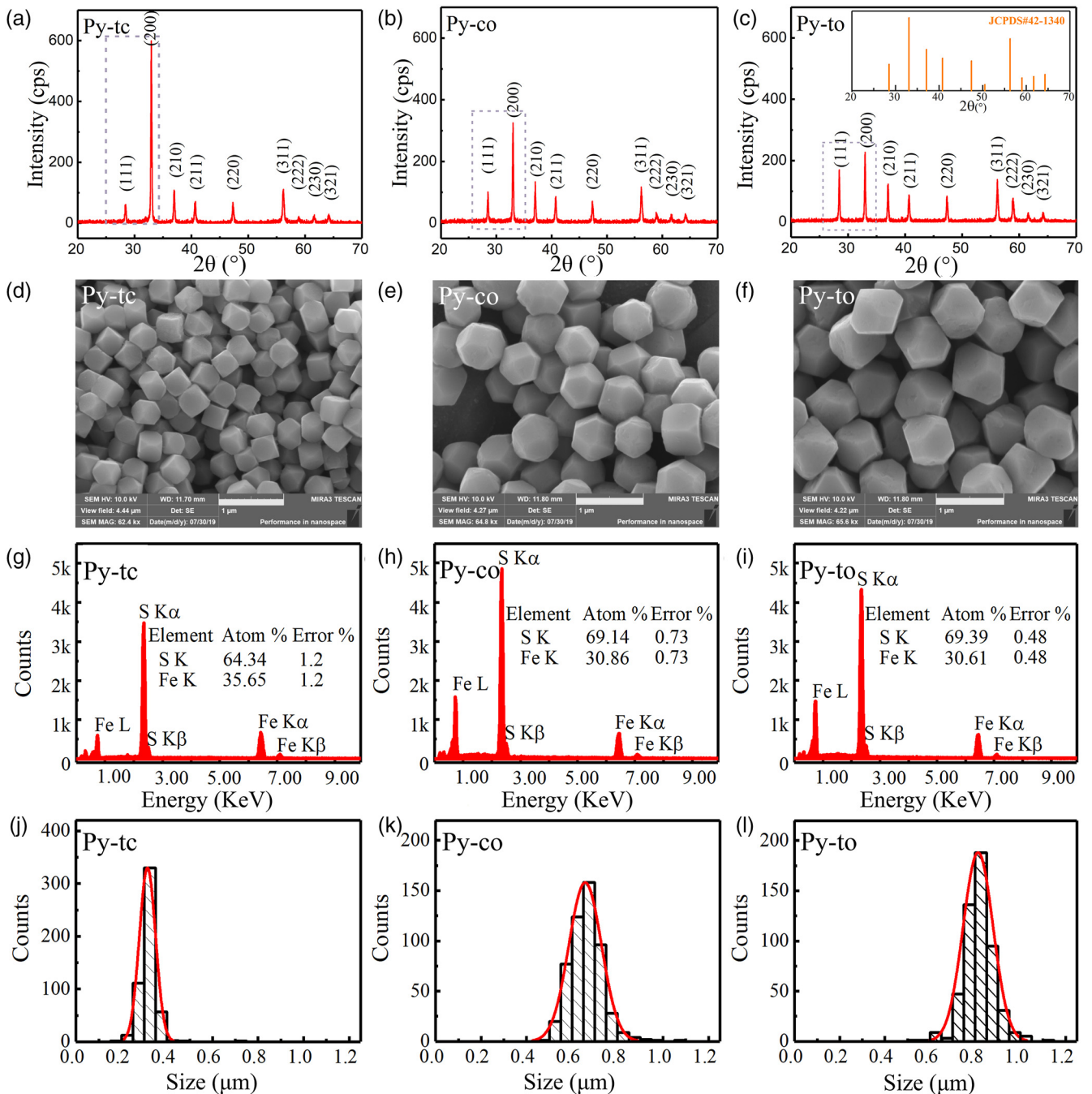


Figure 1 (a–c) X-ray diffraction patterns of synthesised microscopic pyrite samples. (d–f) Field emission scanning electron microscope images of synthesised pyrite samples. (g–i) Energy dispersive spectrometry results of the pyrite samples. The half-quantitative data shown in the spectra were derived from the average measurements of five points. (j–l) Particle size distributions of the pyrite samples, which were derived from the statistical results of at least 500 grains from the micrographs.

signals in the range of 1-2 KeV, which may be due to the introduction of impurities such as Al and Si from the environment in the experimental processes, although their concentrations are less than 0.3 wt. %. EDS results also showed that the Py-co and Py-to samples possessed larger atomic ratios of S to Fe than the Py-tc sample. This was because the Py-co and Py-to samples

possessed larger proportions of {111} facets, which are sulfur-rich surfaces (Alfonso, 2010), than the Py-tc sample.

Statistical analysis based on field emission scanning electron microscope (FESEM) micrographs showed that the average grain sizes of the Py-tc, Py-co, and Py-to samples were 305.0, 641.5 and 801.4 nm, respectively (Fig. 1j-l). According to

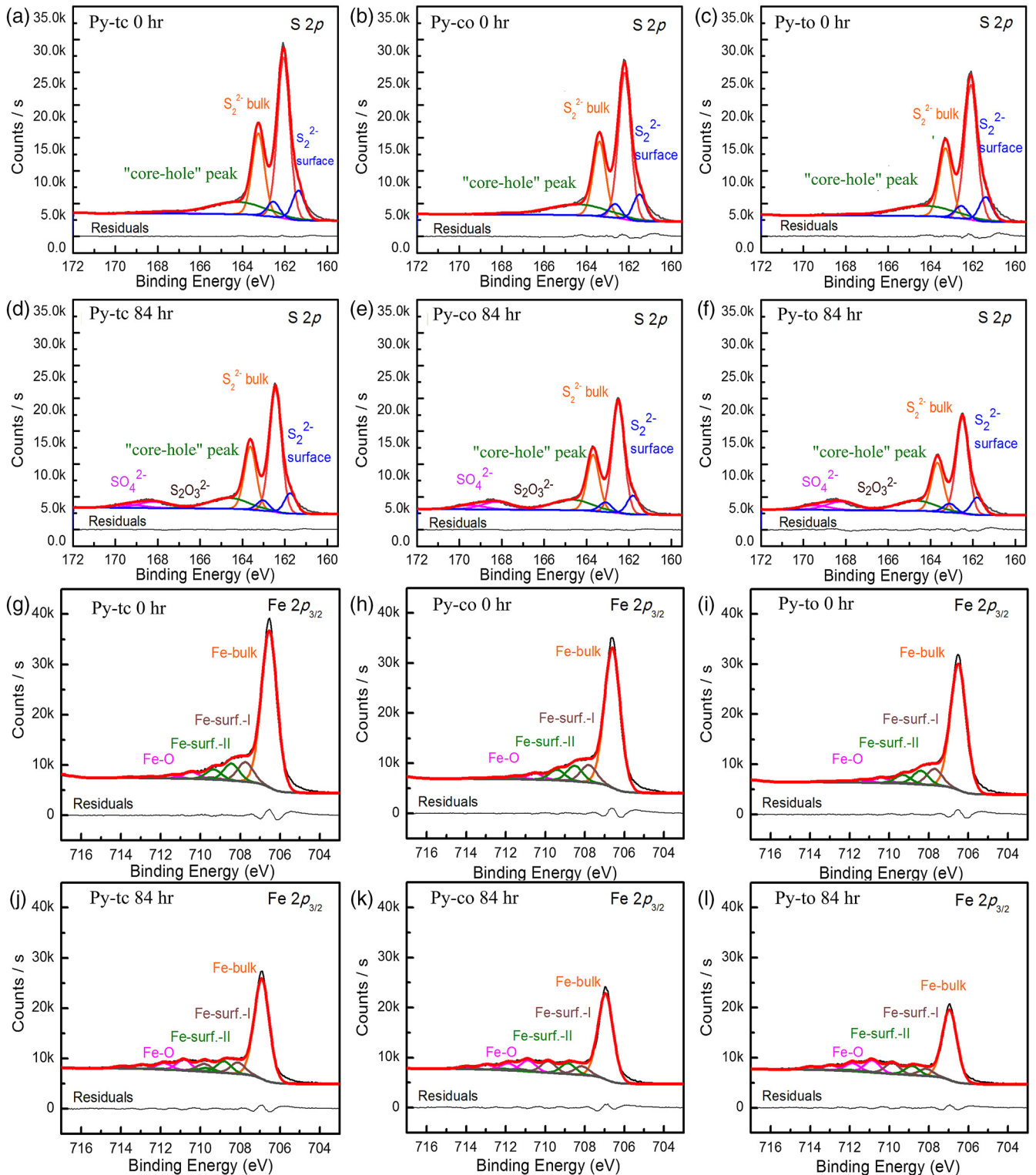


Figure 2 S 2p (a–f) and Fe 2p_{3/2} (g–l) X-ray photoelectron spectroscopy spectra of Py-tc (truncated cubic pyrite), Py-co (cubo-octahedral pyrite), and Py-to (truncated octahedral pyrite) surfaces oxidised in air with a relative humidity of 77 % at intervals of 0 hr and 84 hr. The Fe-surf.-I and Fe-surf.-II denote quadruplet and triplet surface states of iron on pyrite, respectively.



the geometric model (see SI), the SSAs were 2.54, 1.96 and 1.83 m²/g for the Py-tc, Py-co and Py-to samples, respectively.

Oxidation rate of microscopic pyrite with different morphologies. Figure 2 shows the S 2*p* and Fe 2*p*_{3/2} XPS spectra of pyrite before and after oxidation. Here, we used the relative content ratio of oxygen-containing and unoxidised species from the XPS spectra to characterise semi-quantitatively the oxidation rate of the microscopic pyrite (Zhu *et al.*, 2018). The oxygen-containing species from the S 2*p* XPS spectra included sulfate (SO₄²⁻), and the unoxidised species include bulk sulfur (S₂⁻-bulk) and surface sulfur (S₂⁻-surface). The oxygen-containing species from the Fe 2*p* XPS spectra are iron oxides (Fe-O), and the unoxidised species included bulk iron (Fe-bulk) and surface iron (Fe-surf.-I and Fe-surf.-II). The fitting details of S 2*p* and Fe 2*p*_{3/2} XPS spectra are given in the SI.

In addition, the XPS fitting results (Table S-1) showed that thiosulfate was only present at the initial stage of pyrite oxidation, thereby indicating that thiosulfate rapidly converts to sulfate. It is possible that some of these intermediates can be stabilised by impurities in natural pyrites, and thus modify oxidation rates in natural systems. The S/Fe ratio at different oxidation intervals (Table S-2) showed an increasing trend over oxidation time. Because the typical altered product of pyrite is an Fe-sulfate, the S/Fe ratio should be the same. Changes in this ratio may have been caused by concentration or structural changes, or even changes in the newly formed solid phases.

Figure 3a,b shows the kinetic results of the relative content ratios of oxygen-containing species to unoxidised species. The kinetic data from the S 2*p* and Fe 2*p*_{3/2} XPS spectra showed the order of the slope (*k*) for the three samples, *i.e.* $k_{\text{Py-to}} > k_{\text{Py-co}} > k_{\text{Py-tc}}$. Because *k* is proportional to the oxidation rate of pyrite (Zhu *et al.*, 2018), the oxidation rates of the three pyrite samples were in the order $r_{\text{Py-to}} > r_{\text{Py-co}} > r_{\text{Py-tc}}$ (Table S-3). The normalised data (Fig. S-3) also showed the same rate order for the three samples.

The order of the oxidation rate was opposite to that of the SSA [*i.e.* SSA(Py-tc) > SSA(Py-co) > SSA(Py-to)] for the three samples, thereby suggesting that the crystal morphology (*i.e.* surface structure), rather than their fine grain-induced large SSA, controls the reactivity. Therefore, the crystal morphology should be considered in the oxidation process of framboidal pyrite. The estimated oxidation rates of the samples were proportional to the ratio of microscopic pyrite {111} facets to {100} facets (Fig. 3c). Therefore, the oxidation rate of microscopic pyrite {111} facets is greater

than that of {100} facets, which is caused by the difference in surface properties between the {100} and {111} facets (Zhu *et al.*, 2018; Xian *et al.*, 2019). Regardless of grain size, the exposed crystal facet controls the reactivity of the framboidal pyrite microcrystals.

Implications for indicating the local redox conditions of palaeoenvironments. The redox conditions of ancient sediments control the enrichment of biological and redox sensitive trace elements. Pyrite morphology and the size distribution of the framboids are used to indicate palaeoredox conditions (Wilkin and Barnes, 1997a; Wignall *et al.*, 2005; Huang *et al.*, 2016; Liu *et al.*, 2019). Such methods are applicable where there is no oxidative weathering. However, oxidative weathering is always present in ancient sediments. The oxidative products of pyrite, such as magnetite, hematite, limonite, magnesite and goethite, may be the result of pseudomorphism of pyrite (Luther *et al.*, 1982; Wilkin and Barnes, 1997b). Incompletely oxidised pyrite will have a core-shell structure (Courtin-Nomade *et al.*, 2010; Gu *et al.*, 2020). Based on the results of this study, we propose that such a core-shell structure could indicate the relative redox conditions of the palaeoenvironment. This could be a potential proxy for interpreting local redox conditions, such as local oxidation before the Great Oxidation Event (Anbar *et al.*, 2007).

According to the relationship between the shape of the microcrystalline particles and the oxidation rate (Fig. 3c), different crystal facets of oxidised pyrites may form oxidation species with different thicknesses (Fig. 4a). The relative redox conditions of palaeoenvironments where pyrites were present could therefore be characterised by a redox index *p*, as follows:

$$p_{\{hkl\}} = d_{\{hkl\}}/r_{\{hkl\}}$$

where $r_{\{hkl\}}$ is the oxidation rate of a specific pyrite facet {*hkl*} (obtained from Fig. 3c), *i.e.* $r_{\{100\}} = 3.63 \times 10^{-9}$ [mol O₂/m² s] and $r_{\{111\}} = 10.79 \times 10^{-9}$ [mol O₂/m² s], $d_{\{hkl\}}$ is the thickness of the oxidation shell along the {*hkl*} direction. It is worth noting that *p* is a facet-dependent variable. Without consideration of morphology, one may obtain false signals because of the intrinsic oxidation difference between pyrite facets. In practice, a smaller $p_{\{hkl\}}$ value indicates that the degree of pyrite oxidation is relatively weak, whereas a larger $p_{\{hkl\}}$ value denotes a stronger oxidation.

Figure 4b,c showed core-shell structures of two pyrites from a phosphorus deposit. The *p* and *p'* are employed to represent the redox indexes of the two pyrites. The estimated redox

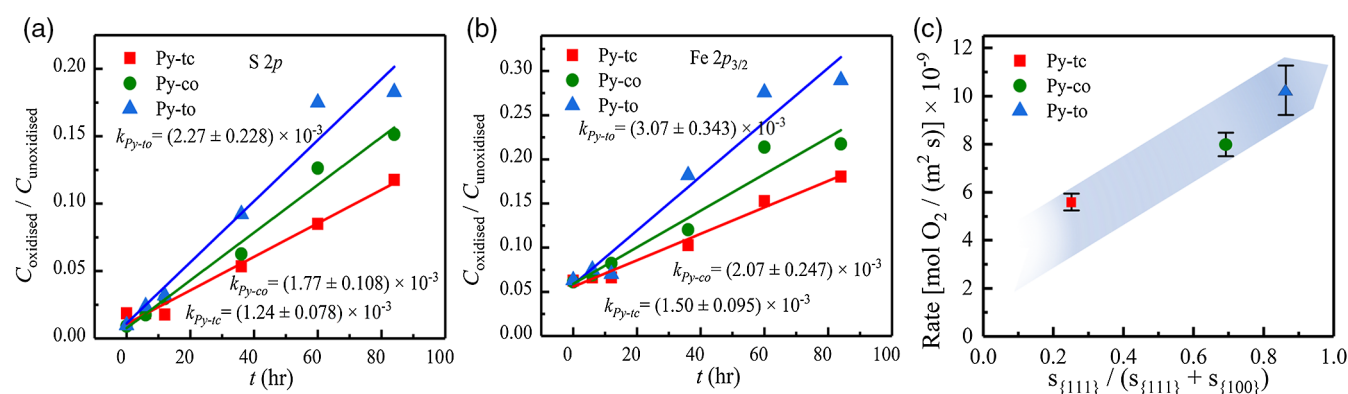


Figure 3 Plots of the concentration ratios of oxidised species to unoxidised species ($C_{\text{oxidised}}/C_{\text{unoxidised}}$) vs. oxidation time (*t*) from (a) S 2*p* and (b) Fe 2*p*_{3/2}. X-ray photoelectron spectroscopy spectra are of Py-tc (truncated cubic pyrite), Py-co (cubo-octahedral pyrite), and Py-to (truncated octahedral pyrite). (c) The estimated oxidation rates of the samples are proportional to the ratio of microscopic pyrite {111} facets to {100} facets.

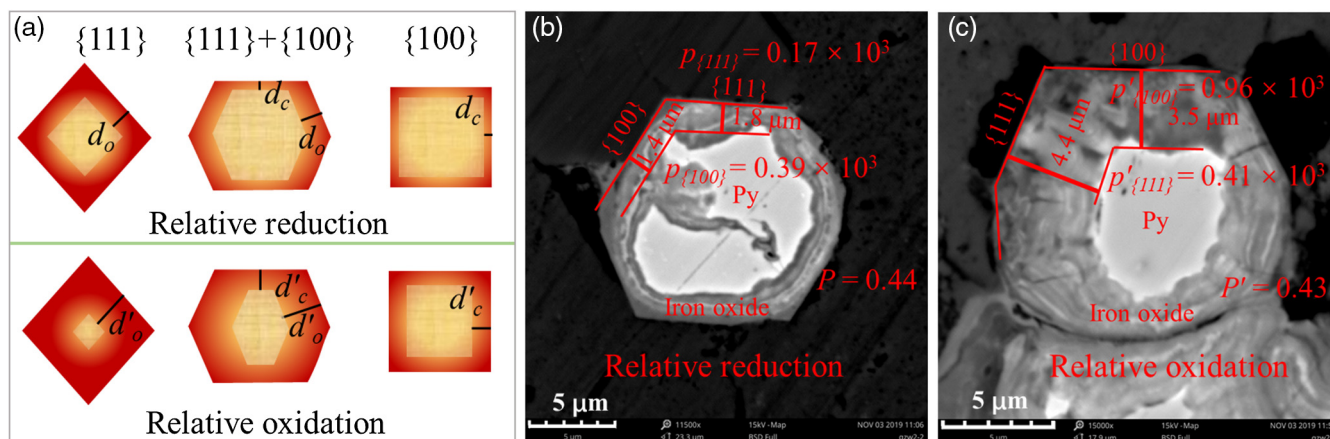


Figure 4 (a) Core-shell models of pyrite with different facets under two redox conditions. The red zone is the oxidised shell and the yellow zone is the unoxidised pyrite core. (b,c) Core-shell morphologies of oxidised natural pyrites from the Zhijin phosphorus deposit in Guizhou Province, China.

indexes are in the order of $p_{\{111\}} < p'_{\{111\}}$, indicating that the latter experienced a more oxidising environment or longer duration of oxidation. Based on the aforementioned definition of the redox index, the p value of all $\{hkl\}$ directions should be the same, e.g., $p_{\{100\}} = p_{\{111\}}$. However, the calculated p values show that $p_{\{100\}} \neq p_{\{111\}}$ and $p'_{\{100\}} \neq p'_{\{111\}}$, which may be caused by the diffusion controlled reaction with the increase in the thickness of oxidation layers. Meanwhile, we introduce another index P ($P = p_{\{111\}}/p_{\{100\}} \leq 1$). In the initial stage of pyrite oxidation, the reaction is fully controlled by surface structure, which gives $P = 1$. With the thickness increase of oxidation products, the reaction is diffusion controlled (the $p_{\{111\}}$ decreases first), resulting in $P < 1$. In addition, because $d_{\{100\}} < d_{\{111\}}$, there is a minimum for P , i.e. $1 > P > r_{\{100\}}/r_{\{111\}} = 0.34$. Therefore, higher P (closer to 1) represent a shorter oxidation duration or lower oxygen fugacity, and thus weaker pyrite oxidation. The index P also works well for the pyrites shown in Figure 4b,c. Moreover, the presence of impurity elements tends to accelerate the oxidation of natural pyrite (Lehner and Savage, 2008), but it will not affect the assessment of local redox conditions of palaeoenvironments if the presence of impurity elements has the same effect on the oxidation of a pyrite crystal in all crystallographic directions.

Acknowledgements

This research was funded by the National Natural Science Foundation of China (Grant No.41825003 and 41921003), Natural Science Foundation of Guangdong Province, China (Grant No. 2019A1515011303), China Postdoctoral Science Foundation (Grant Nos. 2018M643220 and 2019T120755), Guangdong Special Support Program (Grant No. 2019TX05L169), Tuguangchi Award for Excellent Young Scholar GIG, CAS, the Science and Technology Planning Project of Guangdong Province, China (Grant No. 2020B1212060055). This is contribution No. IS-2971 from GIG-CAS.

Editor: Satish Myneni

Additional Information

Supplementary Information accompanies this letter at <https://www.geochemicalperspectivesletters.org/article2104>.



© 2021 The Authors. This work is distributed under the Creative Commons Attribution Non-Commercial No-Derivatives 4.0

License, which permits unrestricted distribution provided the original author and source are credited. The material may not be adapted (remixed, transformed or built upon) or used for commercial purposes without written permission from the author. Additional information is available at <https://www.geochemicalperspectivesletters.org/copyright-and-permissions>.

Cite this letter as: Du, R., Xian, H., Wu, X., Zhu, J., Wei, J., Xing, J., Tan, W., He, H. (2021) Morphology dominated rapid oxidation of framboidal pyrite. *Geochem. Persp. Let.* 16, 53–58.

References

- ALFONSO, D.R. (2010) Computational Investigation of FeS₂ Surfaces and Prediction of Effects of Sulfur Environment on Stabilities. *Journal of Physical Chemistry C* 114, 8971–8980.
- ANBAR, A.D. (2008) Elements and Evolution. *Science* 322, 1481–1483.
- ANBAR, A.D., DUAN, Y., LYONS, T.W., ARNOLD, G.L., KENDALL, B., CREASER, R.A., KAUFMAN, A.J., GORDON, G.W., SCOTT, C., GARVIN, J., BUICK, R. (2007) A Whiff of Oxygen Before the Great Oxidation Event? *Science* 317, 1903–1906.
- COURTIN-NOMADE, A., BRIL, H., BÉNY, J.-M., KUNZ, M., TAMURA, N. (2010) Sulfide oxidation observed using micro-Raman spectroscopy and micro-X-ray diffraction: The importance of water/rock ratios and pH conditions. *American Mineralogist* 95, 582–591.
- FAKHRAEE, M., HANCISSE, O., CANFIELD, D.E., CROWE, S.A., KATSEV, S. (2019) Proterozoic seawater sulfate scarcity and the evolution of ocean-atmosphere chemistry. *Nature Geoscience* 12, 375–380.
- FIKE, D.A., BRADLEY, A.S., ROSE, C.V. (2015) Rethinking the Ancient Sulfur Cycle. *Annual Review of Earth and Planetary Sciences* 43, 593–622.
- GU, X., HEANEY, P.J., REIS, F.D.A.A., BRANTLEY, S.L. (2020) Deep abiotic weathering of pyrite. *Science* 370, doi: 10.1126/science.abb8092.
- GUY, B.M., BEUKES, N.J., GUTZMER, J. (2010) Paleoenvironmental controls on the texture and chemical composition of pyrite from non-conglomeratic sedimentary rocks of the Mesoproterozoic Witwatersrand Supergroup, South Africa. *South African Journal of Geology* 113, 195–228.
- HALLBAUER, D.K. (1986) The mineralogy and geochemistry of Witwatersrand pyrite gold, uranium and carbonaceous matter mineral deposits of South Africa. In: ANHAUESSER, C.R., MASKE, S. (Eds.) *Mineral Deposits of Southern Africa*. Geological Society of South Africa, South Africa, Vol. 1, 731–752.
- HAYAKAWA, A., HATAKEYAMA, M., ASANO, R., ISHIKAWA, Y., HIDAKA, S. (2013) Nitrate reduction coupled with pyrite oxidation in the surface sediments of a



- sulfide-rich ecosystem. *Journal of Geophysical Research: Biogeosciences* 118, 639–649.
- HUANG, Y., CHEN, Z.-Q., WIGNALL, P.B., ZHAO, L. (2016) Latest Permian to Middle Triassic redox condition variations in ramp settings, South China: Pyrite framboid evidence. *Geological Society of America Bulletin* 129, 15.
- KOZINA, N., REYKHARD, L., DARA, O., GORDEEV, V. (2018) Framboidal pyrite formation in the bottom sediments of the South Caspian Basin under conditions of hydrogen sulfide contamination. *Russian Journal of Earth Sciences* 18, 1–10.
- LEHNER, S., SAVAGE, K. (2008) The effect of As, Co, and Ni impurities on pyrite oxidation kinetics: Batch and flow-through reactor experiments with synthetic pyrite. *Geochimica et Cosmochimica Acta* 72, 1788–1800.
- LIU, Z., CHEN, D., ZHANG, J., LU, X., WANG, Z., LIAO, W., SHI, X., TANG, J., XIE, G. (2019) Pyrite Morphology as an Indicator of Paleoredox Conditions and Shale Gas Content of the Longmaxi and Wufeng Shales in the Middle Yangtze Area, South China. *Minerals* 9, 428.
- LUTHER, G.W., GIBLIN, A., HOWARTH, R.W., RYANS, R.A. (1982) Pyrite and Oxidized Iron Mineral Phases Formed from Pyrite Oxidation in Salt-Marsh and Estuarine Sediments. *Geochimica et Cosmochimica Acta* 46, 2665–2669.
- OHFUJI, H., RICKARD, D. (2005) Experimental syntheses of framboids—a review. *Earth-Science Reviews* 71, 147–170.
- PUGH, C.E., HOSSNER, L.R., DIXON, J.B. (1984) Oxidation rate of iron sulfides as affected by surface area, morphology, oxygen concentration and autotrophic bacteria. *Soil Science* 137, 309–314.
- RICKARD, D. (2012) *Sulfidic Sediments and Sedimentary Rocks*. Elsevier, Amsterdam, Netherlands.
- RICKARD, D. (2015) *Pyrite: A Natural History of Fool's Gold*. Oxford University Press, New York.
- RICKARD, D. (2019a) How long does it take a pyrite framboid to form? *Earth and Planetary Science Letters* 513, 64–68.
- RICKARD, D. (2019b) Sedimentary pyrite framboid size-frequency distributions: A meta-analysis. *Palaeogeography, Palaeoclimatology, Palaeoecology* 522, 62–75.
- RICKARD, D., MUSSMANN, M., STEADMAN, J.A. (2017) Sedimentary Sulfides. *Elements* 13, 117–122.
- RIGBY, P.A., DOBOS, S.K., COOK, F.J., GOONETILLEKE, A. (2006) Role of organic matter in framboidal pyrite oxidation. *Science of The Total Environment* 367, 847–854.
- SAWLOWICZ, Z. (2000) *Framboids: From their origin to application*. Prace Mineralogiczne, Kraków, Poland.
- WANG, P., TIAN, J., HUANG, E. (2018) *Earth system and evolution*. Science Press, Beijing.
- WEBER, P.A., STEWART, W.A., SKINNER, W.M., WEISNER, C.G., THOMAS, J.E., SMART, R.St.C. (2004) Geochemical effects of oxidation products and framboidal pyrite oxidation in acid mine drainage prediction techniques. *Applied Geochemistry* 19, 1953–1974.
- WIGNALL, P.B., NEWTON, R., BROOKFIELD, M.E. (2005) Pyrite framboid evidence for oxygen-poor deposition during the Permian–Triassic crisis in Kashmir. *Palaeogeography, Palaeoclimatology, Palaeoecology* 216, 183–188.
- WILKIN, R.T., BARNES, H.L. (1997a) Pyrite formation in an anoxic estuarine basin. *American Journal of Science* 297, 620–650.
- WILKIN, R.T., BARNES, H.L. (1997b) Formation processes of framboidal pyrite. *Geochimica et Cosmochimica Acta* 61, 323–339.
- WILKIN, R.T., BARNES, H.L., BRANTLEY, S.L. (1996) The size distribution of framboidal pyrite in modern sediments: An indicator of redox conditions. *Geochimica et Cosmochimica Acta* 60, 3897–3912.
- XIAN, H., HE, H., ZHU, J., DU, R., WU, X., TANG, H., TAN, W., LIANG, X., ZHU, R., TENG, H. (2019) Crystal habit-directed gold deposition on pyrite: Surface chemical interpretation of the pyrite morphology indicative of gold enrichment. *Geochimica et Cosmochimica Acta* 264, 191–204.
- ZHU, J., XIAN, H., LIN, X., TANG, H., DU, R., YANG, Y., ZHU, R., LIANG, X., WEI, J., TENG, H., HE, H. (2018) Surface structure-dependent pyrite oxidation in relatively dry and moist air: Implications for the reaction mechanism and sulfur evolution. *Geochimica et Cosmochimica Acta* 228, 259–274.

Morphology dominated rapid oxidation of framboidal pyrite

R. Du, H. Xian, X. Wu, J. Zhu, J. Wei, J. Xing, W. Tan, H. He

Supplementary Information

The Supplementary Information includes:

- Materials and Methods
- Supplementary Text: Calculation of specific surface area; surface species on the microscopic pyrite
- Tables S-1 to S-3: S $2p$ peak parameters and chemical states of oxidised pyrites, S/Fe ratios derived from X-ray photoelectron spectroscopy (XPS) survey spectra at different oxidation intervals, and a comparison of oxidation rates of the samples.
- Figures S-1 to S-3: S $2p$ spectra and Fe $2p_{3/2}$ XPS spectra of oxidised Py-tc, Py-co and Py-to surfaces and the kinetic data normalised by the SSAs of the three samples.
- Supplementary Information References

Materials and Methods

Preparation of microscopic pyrite

Highly pure microscopic pyrite samples were synthesised using a polymer-assisted hydrothermal method which was modified after Wang *et al.* (2010). The process was performed in a glove box (MIKROUNA) fulfilled with high-pure nitrogen (>99.99 %), 21 mL polyvinyl alcohol solution (4.4 wt. %) and 0.45 g polyvinylpyrrolidone were dissolved in 39 mL water, then 0.4 g $\text{FeCl}_2 \cdot 4\text{H}_2\text{O}$ was added to this solution under constant stirring to form a homogeneous mixture. 10 mL NaOH (0.7 M) was added dropwise into the mixture, and finally 0.4 g Sulfur powder was added to the solution under magnetic stirring for 1 hour. By appropriately increasing the amount of NaOH (0.7 M) from 10 mL to 11 mL, microcrystalline pyrite with different morphologies containing {100} and {111} crystal facets finally can be synthesised. The above reagents are of analytical grade. The mixture was sealed in a Teflon-lined stainless-steel autoclave (70 % filled), and maintained at 453 K for 12 h, then cooled to room temperature naturally. The products were washed 3 times with Milli-Q water and 3 times with anhydrous ethanol. The collected samples were dried at 60° under vacuum, and then stored in the glove box with nitrogen atmosphere.

Oxidation experiments

The samples possessing similar morphology with framboidal pyrite microscopic crystals were used to conduct oxidation experiments in 77 $R_h\%$ air. Glass slides with covered pyrite film were employed to the oxidation experiments, which was prepared in the oxygen-insulated glove box. The pyrite films were prepared by dropping suspension on glass slides, the suspension composed of the pyrite samples and ethanol. The oxidation experiments were carried out in an airtight homemade reaction cell at room temperature. Saturated NaCl solution was used to control the humidity condition, providing a relative humidity of 77 $R_h\%$ throughout the experiments.

Characterisation

The X-ray diffraction (XRD) patterns were recorded on a Bruker D8 ADVANCE X-ray diffractometer with a Ni filter and Cu $K\alpha$ radiation source, which were operated at a generator voltage of 40 kV and a current of 40 mA. The chemical composition and morphology of the samples were analysed on a MIRA3 TESCAN field emission scanning electron microscope (FESEM) equipped with the energy dispersive spectrometry (EDS). The working distance of the EDS analysis was set at 6.5 mm. Thin sections of natural pyrite samples were prepared for scanning electron microscopy (SEM) observations using a Phenom XL SEM equipped with a back-scattered electron (BSE) detector. X-ray photoelectron spectroscopic (XPS) analysis on a Thermo Scientific K-alpha spectrometer with a base pressure of 10^{-8} mbar and an aluminium $K\alpha$ source (1486.8 eV). The spectra were processed using the Thermo Avantage analysis software with smart backgrounds and peaks with mixed Lorentz-Gaussian shapes.

Supplementary Text

Calculation of specific surface area

Because the limited amount of synthesised samples restricted the use of the N_2 adsorption BET method to determine their SSA, the SSAs of the pyrite samples were estimated based on geometry, as follows:

$$S = s / V \rho,$$

where S is the SSA, s and V are the surface area and volume of the grains, respectively, and ρ is the density of pyrite (5 g/cm^3). The geometric lengths required in the calculations were derived from the average value of the statistical measurements from a series of FESEM micrographs (Fig. 1j–l). According to the geometric model, the SSAs were 2.54, 1.96 and 1.83 m^2/g for the Py-tc, Py-co and Py-to samples, respectively.

Surface species on the microscopic pyrite

S $2p$ and Fe $2p_{3/2}$ XPS spectra are utilized to characterize surface states of pyrite before and after oxidation (Herbert *et al.*, 2014; Zhu *et al.*, 2018; Xian *et al.*, 2019). From XPS S $2p$ spectra of the pyrite samples before and after oxidization for 84 hours (Fig. S-1), two doublets, with maxima at 162.50 and 161.80 eV are assigned to the bulk sulfur dimer (S_2^{2-} -bulk) and the surface sulfur dimer (S_2^{2-} -surface), respectively. The tail feature at 164.40 eV is generated by the core-hole effect in pyrite (Herbert *et al.*, 2014). Two doublets, with maxima at 166.60 and 168.20 eV are assigned to the thiosulphate ($S_2O_3^{2-}$) and sulphate (SO_4^{2-}) on the surface of oxidised pyrite, respectively. The results (Table S-1) showed that thiosulphate only present at the initial stage of pyrite oxidation, thereby indicating that thiosulfate rapidly converts to sulphate. From XPS Fe $2p_{3/2}$ spectra of the pyrite samples before and after oxidisation for 84 hours (Fig. S-2), the low spin bulk Fe at 706.60 eV and two surface Fe states were observed. One surface Fe state is a quadruplet with a minimum at 707.20 eV, and the other one is a triplet with a minimum at 708.50 eV. A quadruplet with minima at 710.80 eV is assigned to Fe (III)-O type species. The peaks of sulphate and iron oxyhydroxides increase with the oxidation time (Figs. S-1 and S-2), indicating the increase of their content on the surface of pyrite samples.



Supplementary Tables

Table S-1 S 2p peak parameters and chemical states of oxidised pyrites.

Samples	Species	$\Delta E_B/eV$	Percentage of species detected					
			0 hr	6 hr	12 hr	36 hr	60 hr	84 hr
Py-tc	Bulk S	0						
	Doublet	1.2	75.58	77.01	74.92	73.09	71.57	70.93
	Surf S	-0.7						
	Doublet	0.5	13.82	13.98	13.45	12.43	12.06	11.59
	CH	2.18	10.54	9.00	11.41	12.07	11.61	10.74
	Sulfate	5.7						
	Doublet	6.9	0.00	0.00	0.22	2.41	4.76	6.73
	Thiosulfate Doublet	4.05 5.25	0.07	0.00	0.00	0.00	0.00	0.00
Py-co	Bulk S	0						
	Doublet	1.2	74.33	74.68	74.41	72.87	69.58	67.88
	Surf S	-0.7						
	Doublet	0.5	13.84	13.56	13.23	13.15	11.91	11.63
	CH	2.18	11.79	11.12	11.09	11.13	11.58	11.67
	Sulfate	5.7						
	Doublet	6.9	0.00	0.11	0.83	2.63	6.83	8.81
	Thiosulfate Doublet	4.05 5.25	0.03	0.53	0.45	0.23	0.11	0.00
Py-to	Bulk S	0						
	Doublet	1.2	74.31	75.13	73.42	71.48	64.39	65.01
	Surf S	-0.7						
	Doublet	0.5	14.20	13.83	13.47	12.97	11.98	11.75
	CH	2.18	11.49	10.79	11.87	11.28	12.87	12.09
	Sulfate	5.7						
	Doublet	6.9	0.00	0.00	0.84	4.14	10.76	11.15
	Thiosulfate Doublet	4.05 5.25	0.00	0.25	0.40	0.12	0.00	0.00

Table S-2 S/Fe ratios derived from X-ray photoelectron spectroscopy (XPS) survey spectra at different oxidation intervals.

Samples	S/Fe ratio (XPS survey spectra)					
	0 hr	6 hr	12 hr	36 hr	60 hr	84 hr
Py-tc	3.29	3.27	3.47	3.69	3.94	4.12
Py-co	3.38	3.52	3.55	3.61	3.40	3.42
Py-to	3.71	3.58	3.72	4.14	3.92	3.83



Table S-3 Comparison of oxidation rates of Py-tc, Py-co and Py-to.

Samples	Rate (mol O ² /m ² s)	
	<i>r</i> S _{2p}	<i>r</i> Fe 2p _{3/2}
Py-tc	$(5.595 \pm 0.3520) \times 10^{-9}$	$(6.768 \pm 0.4287) \times 10^{-9}$
Py-co	$(7.987 \pm 0.4873) \times 10^{-9}$	$(9.340 \pm 1.1145) \times 10^{-9}$
Py-to	$(1.024 \pm 0.1029) \times 10^{-8}$	$(1.385 \pm 0.1548) \times 10^{-8}$

Calculation methods refer to the literature (Zhu *et al.*, 2018).



Supplementary Figures

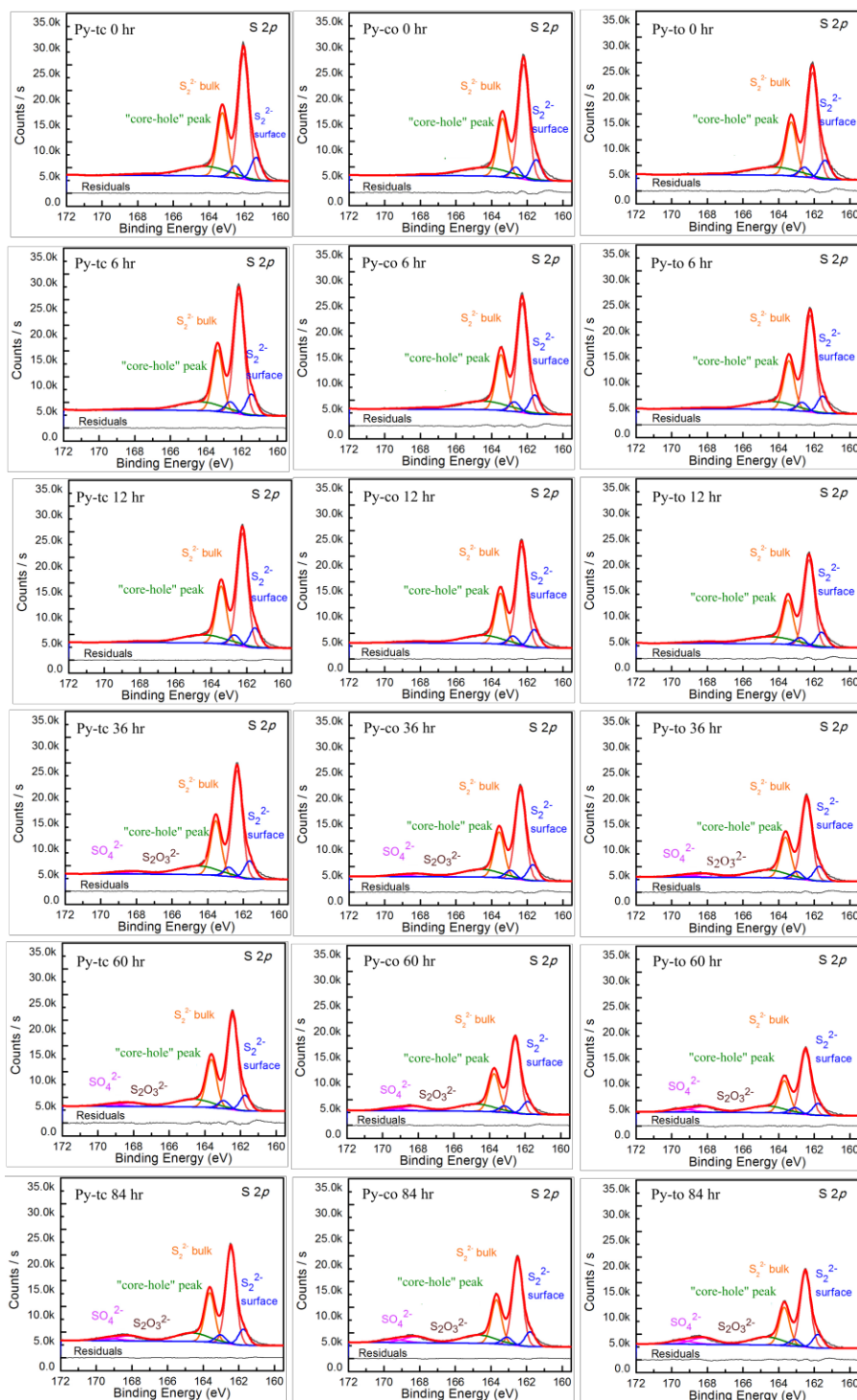


Figure S-1 S2p X-ray photoelectron spectroscopy spectra of pyrite Py-tc (truncated cubic pyrite), Py-co (cubooctahedral pyrite), and Py-to (truncated octahedral pyrite) surfaces oxidised in air with a relative humidity of 77 % at intervals of 0, 6, 12, 36, 60 and 84 hr.



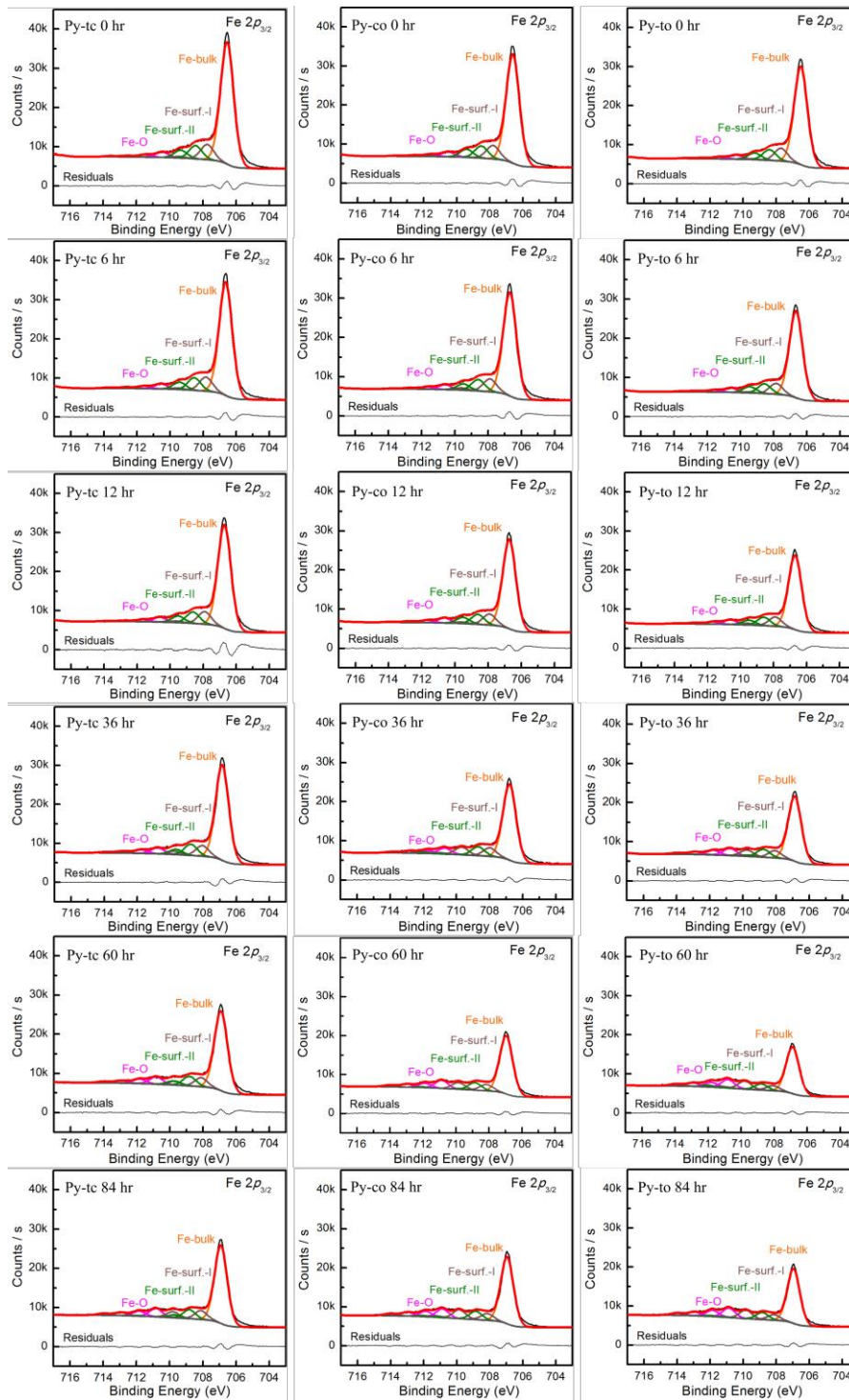


Figure S-2 Fe $2p_{3/2}$ X-ray photoelectron spectroscopy spectra of pyrite Py-tc (truncated cubic pyrite), Py-co (cubooctahedral pyrite), and Py-to (truncated octahedral pyrite) surfaces oxidised in air with a relative humidity of 77 % at intervals of 0, 6, 12, 36, 60 and 84 hr.

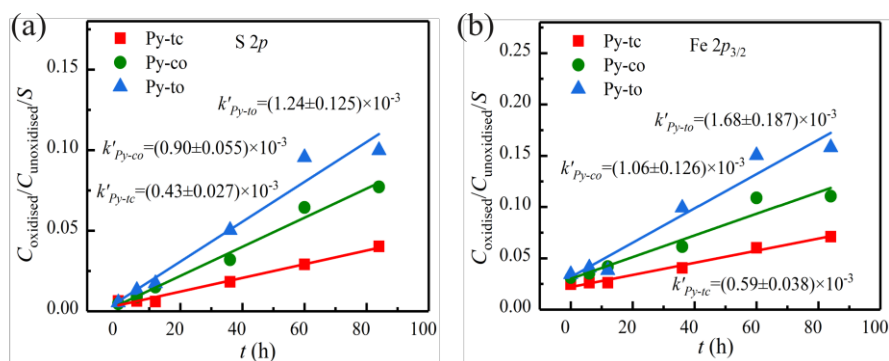


Figure S-3 The kinetic data normalised by SSA of the three samples. k' vs. oxidation time (t) from S 2p (a) and Fe 2p_{3/2} (b) XPS spectra of pyrite Py-tc, Py-co and Py-to oxidised surfaces. k' is the concentration ratio of oxygen-containing species to unoxidised species ($C_{\text{oxidised}}/C_{\text{unoxidised}}/SSAs$).

Supplementary Information References

- Herbert, F.W., Krishnamoorthy, A., Ma, W., Van Vliet, K.J., Yildiz, B. (2014) Dynamics of point defect formation, clustering and pit initiation on the pyrite surface. *Electrochimica Acta* 127, 416–426.
- Wang, D., Wang, Q., Wang, T. (2010) Controlled growth of pyrite FeS 2 crystallites by a facile surfactant-assisted solvothermal method. *CrystEngComm* 12, 755–761.
- Xian, H., He, H., Zhu, J., Du, R., Wu, X., Tang, H., Tan, W., Liang, X., Zhu, R., Teng, H. (2019) Crystal habit-directed gold deposition on pyrite: Surface chemical interpretation of the pyrite morphology indicative of gold enrichment. *Geochimica et Cosmochimica Acta* 264, 191–204.
- Zhu, J., Xian, H., Lin, X., Tang, H., Du, R., Yang, Y., Zhu, R., Liang, X., Wei, J., Teng, H., He, H. (2018) Surface structure-dependent pyrite oxidation in relatively dry and moist air: Implications for the reaction mechanism and sulfur evolution. *Geochimica et Cosmochimica Acta* 228, 259–274.

